11-1-2023

Grain boundary and texture evolution of TiB/Ti–2Al–6Sn titanium matrix composite under electroshocking treatment

Yaya Wu

Yan Wen

Anan Guo

Jian Zhou

Fei Yin

See next page for additional authors

10.1016/j.jmrt.2023.10.177

Wu, Y., Wen, Y., Guo, A., Zhou, J., Yin, F., Xie, L., . . . Zhang, L. C. (2023). Grain boundary and texture evolution of TiB/Ti–2Al–6Sn titanium matrix composite under electroshocking treatment. Journal of Materials Research and Technology, 27, 4305-4316. https://doi.org/10.1016/j.jmrt.2023.10.177

Journal of Materials Research and Technology 27 (2023) 4305–4316

Contents lists available at ScienceDirect

Journal of Materials Research and Technology

journal homepage: www.elsevier.com/locate/jmrt

Grain boundary and texture evolution of TiB/Ti–2Al–6Sn titanium matrix composite under electroshocking treatment

Yaya Wu [a,b,1], Yan Wen [a,b,1], Anan Guo [c], Jian Zhou [a,b], Fei Yin [a,b], Lechun Xie [a,b,*], Liqiang Wang [d], Lin Hua [a,b,c,**], Weijie Lu [d], Lai-Chang Zhang [e]

[a] Hubei Key Laboratory of Advanced Technology for Automotive Components, Wuhan University of Technology, Wuhan 430070, PR China
[b] Hubei Collaborative Innovation Center for Automotive Components Technology, Wuhan 430070, PR China
[c] State Key Laboratory of Advanced Technology for Materials Synthesis and Processing, Wuhan University of Technology, Wuhan, 430070, China
[d] State Key Laboratory of Metal Matrix Composites, School of Materials Science and Engineering, Shanghai Jiao Tong University, Shanghai 200240, PR China
[e] School of Engineering, Edith Cowan University, Joondalup, Perth, WA 6027, Australia

ARTICLE INFO

Keywords:
Electroshocking treatment (EST)
TiB/Ti–2Al–6Sn
Microstructure
Reinforcement
Phase content
Texture

ABSTRACT

This work used electroshocking treatment (EST) plus external loading to regulate the microstructure of titanium matrix composites (TMCs). The external loading was 0.3 MPa. After EST plus external loading with 0.3 MPa, the α was reduced to 2.53 μm in size. The percentage of high angle grain boundaries (HAGBs) in α increased first and then decreased. The percent of HAGBs in TiB decreased, mainly due to the introduction of abundant dislocations in the TiB/matrix interface after EST. After EST, the maximum texture strength of TiB decreased from 13.09 to 12.97, and that of α decreased from 3.11 to 1.58. After EST under external loading with 0.3 MPa, the maximum texture strength of TiB decreased to 8.10. The orientation of TiB experienced significant variation. TEM results showed that TiB and α formed a distorted interface after EST under external loading with 0.3 MPa. The interplanar spacing of TiB and α was varied. All results show that the texture of TMCs can be relieved by EST plus external loading with 0.3 MPa. It is mainly attributed to the thermal and athermal effects and the imposed external loads with EST. EST plus external loading provides a new method for manipulating the microstructure of TMCs.

1. Introduction

Titanium matrix composites (TMCs) are widely used in aerospace, automotive and military fields due to their high temperature resistance and high specific strength [1–9]. Some researchers have shown that the mechanical properties of TMC are closely related to its microstructure and texture [10]. Therefore, a deep understanding of the microstructure evolution of TMCs is of great theoretical significance for the wider application of TMCs. It is known that the properties of TMCs are closely related to their microstructure and texture. It was reported that the microstructure and mechanical properties of TMCs could be altered through different treatments [11,12].

Sasaki et al. [13] stated that α-Ti precipitated on two different TiB planes after heat treatment in β-stabilized Ti–15Mo-2.6Nb–3Al-0.2Si-0.12B, and multiple orientation relationships between α and TiB were found. Shibayan et al. [14] investigated that the regular β-grains of the extruded Ti–6Al–4V-0.1B consisted of fine pristine β-grains and acicular β-flakes with a stable microstructure. Wen et al. [15] showed that the nanocrystalline grains and high dislocation density were formed in the nanocrystalline layer, and the compressive residual stress and hardness of the shot peened surface were improved after shot peening on (TiB + TiC)/Ti–6Al–4V. Indrani et al. [16] found that due to the strain incompatibility between the matrix and TiB, dislocations and twins were generated during the cyclic loading process, which reduced the cyclic stress-strain. Zhang et al. [17] showed that the new Ti–Al –Sn alloy exhibited the highest ultimate tensile strength and yield strength after heat treatment, with the precipitation of a second phase at a certain solution temperature. As the solution temperature increased, the size of the precipitated phase increased. Yu et al. [18] found that TiBw/Ti–6Al–4V after heat treatment, the fine α+β The size

* Corresponding author. Hubei Key Laboratory of Advanced Technology for Automotive Components, Wuhan University of Technology, Wuhan 430070, PR China.
** Corresponding author. Hubei Key Laboratory of Advanced Technology for Automotive Components, Wuhan University of Technology, Wuhan 430070, PR China.
E-mail addresses: xielechun@whut.edu.cn, lechunxie@yahoo.com (L. Xie), hualin@whut.edu.cn (L. Hua).
[1] These authors contributed equally.

https://doi.org/10.1016/j.jmrt.2023.10.177
Received 2 August 2023; Accepted 16 October 2023
Available online 21 October 2023

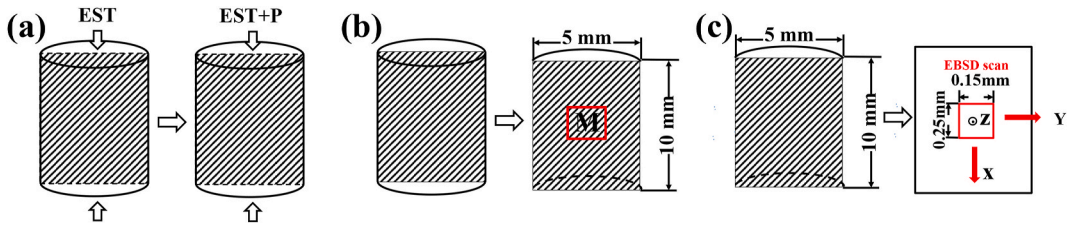

Fig. 1. Schematic diagrams of: (a) specimen under EST and EST plus loading *P*, (b) microstructure characterization area for SEM and TEM, and (c) microstructure characterization area of EBSD.

Table 1
Specimens number and EST parameters under different loading.

Specimen number	EST time(s)	*P* (MPa)
No.1	0	0
No.2	0.06	0
No.3	0.06	0.3

of the phase increases with the increase of aging temperature, and the mechanical properties increase with the increase of temperature. The mechanical properties at high temperature and room temperature are different. Huang et al. [19] studied that the in-situ TiBw reinforced TC4 composite material has continuous reinforcement network distribution, and the network boundary generated strengthening effect at high temperature. It is the main reason for the significant improvement of room temperature/high temperature tensile properties. Huang et al. [20] showed that TiBw/Ti–6Al–4V after by hot pressing sintering can increase tensile strength.

Wang et al. [21] reported that the extruded composite material exhibited a strong $(0001)_{\alpha}$//extrusion direction fiber texture, which was transformed from the $(110)_{\beta}$//extrusion direction fiber texture based on the Burgers relationship, which was beneficial to the tensile properties of TMCs. Hill et al. [10] reported the orientation relationship between equiaxed α and TiB precipitation as $(0001)_{\alpha}//(001)_{TiB}$ and $[1120]_{\alpha}//[010]_{TiB}$. Ni et al. [22] indicated that the position of TiC particles and TiB whiskers were relatively fixed, and TiCp tended to grow on the $(101)_{TiB}$ plane. The (0002) pole figure of rolled Ti–6Al–4V showed the "TD splitting" at lower rolling temperature [23]. Huang et al. [24] found that the particle-induced nucleation (PSN) behavior of TiB particles caused the recrystallized grains of different orientations to nucleate around a single TiB particle through random lattice rotation. Lu et al. [25] showed that the orientation relationship between TiB and Ti is related to the solidification path and growth mechanism of TiB. Saito et al. [26] reported that TiB reinforced titanium alloys exhibit excellent mechanical properties at high temperatures up to 1100K. Li et al. [27] demonstrated that SLM-fabricated 2 vol% TiB/Ti–6Al–4V has a higher yield strength (1345 MPa) and a significant increase in fracture strain to 31.3 %.Wu et al. [28] stated that short and thick TiB whiskers in Ti–5Mo–5V–8C–3Al alloy, and the boronized Ti–5Mo–5V–8Cr–3Al alloy has better wear resistance than the original alloy. Yang et al. [29] researched that the growth and morphology of TiB are closely related to the surface properties of titanium alloys. The above studies show that the grain size of TMCs decreases and the texture strength changes after heat treatment, which can improve its comprehensive properties to a certain extent. Although a reasonable heat treatment process can effectively improve the mechanical properties of TMCs, the energy utilization rate of the heat treatment process is low.

In recent years, electroshocking treatment (EST) has attracted attention by many researchers due to its low energy consumption, short processing time, and targeted treatment. Song et al. [30] demonstrated that EST accelerated the movement of dislocations and reduced the dislocation density from 2.37×10^{15} m^{-2} to 1.96×10^{15} m^{-2}, thereby promoting local recrystallization, and the typical deformation texture was significantly weakened. Wu et al. [31] investigated that refined and spheroidized primary α phase was obtained in Ti-6.6Al-3.4Mo after EST. Liu et al. [32] indicated that Ti-6.5Al-3.5Mo-1.5Zr-0.3Si (TC11) alloy underwent phase transformation and dislocations accumulated at the boundary to form defects after EST, which declined strength of the alloy. Xie et al. [33] demonstrated that EST can refine TiB from micrometers to nanometers in TiB/Ti–2Al–6Sn. Xie et al. [34] found that the porosity of laser melting deposited β-titanium alloys decreased significantly from 0.81 % to 0.1 % after EST. The maximum texture strength of β phase decreased from 23.18 to 13.15 after EST in near-β titanium alloy, and the texture strength had uniform distribution [35]. Besides, the microstructure of TC11 titanium alloys changed after EST, the α texture intensity increased from 4.94 to 8.52, and that of β phase increased from 3.35 to 9.88 [36]. In summary, previous studies mainly focused on the microstructure variation and mechanical properties of TMCs after EST. However, the influencing mechanism of EST on the evolution of grain boundaries, texture and the phase content of TiB reinforced TMCs are still unclear and need further investigation.

In this work, the advantages of EST and a specific external loading are applied synchronously during EST for tailoring the microstructure and mechanical properties of TiB/Ti–2Al–6Sn. The variation of texture, grain size, and grain orientation of α phase and TiB are analyzed by Electron Backscattered Diffraction (EBSD) in detail. Furthermore, the evolution mechanism is discussed based on the results, which can provide new ideas and methods for processing TMCs.

2. Experimental

2.1. Specimens preparation and EST experiments

In this work, 8 % TiB particle-reinforced TiB/Ti–2Al–6Sn was synthesized by in situ method [33]. Before EST, a cylindrical specimen with a diameter of 5 mm and a length of 10 mm was processed by wire-electrode cutting. In order to perform the EST experiments, the surface oxide layer on specimen was removed. Note that, the top and bottom surfaces of the cylindrical specimen were smooth to ensure that both surfaces of the specimen were in full contact with the two electrodes of the EST equipment. The mere EST with 0.06 s and the EST with 0.06 s plus an external loading of 0.3 MPa were applied on specimens, and the schematic is shown in Fig. 1(a). Because the external load (*P*) was low, the load was directly applied to the upper surface of copper electrode. The specimen number and processing parameters are shown in Table 1. The untreated specimen was marked as No.1, the specimen with mere EST as No.2 and the specimen with EST plus the external loading as No.3. The EST current amplitude and density were 4.5×10^3 A and 2.3×10^4 A/cm^2, respectively. The EST pulse voltage signal monitored by the Hall current sensor was 7.8×10^3 mV. The detailed EST process can be found in our previous works [32,33]. The oxide-removed sample was placed between two copper electrodes in the EST device, and the upper and lower surfaces of specimens were in contact with the electrodes. The temperature change of specimens during EST was detected by Fotric Infrared Imager. The distance between the infrared thermal imager and the sample is 20 cm, and the focus is kept clear at a room temperature of 20 °C. Infrared thermal imager (Fotric-220) response wavelength is 8–14 μm, choose the

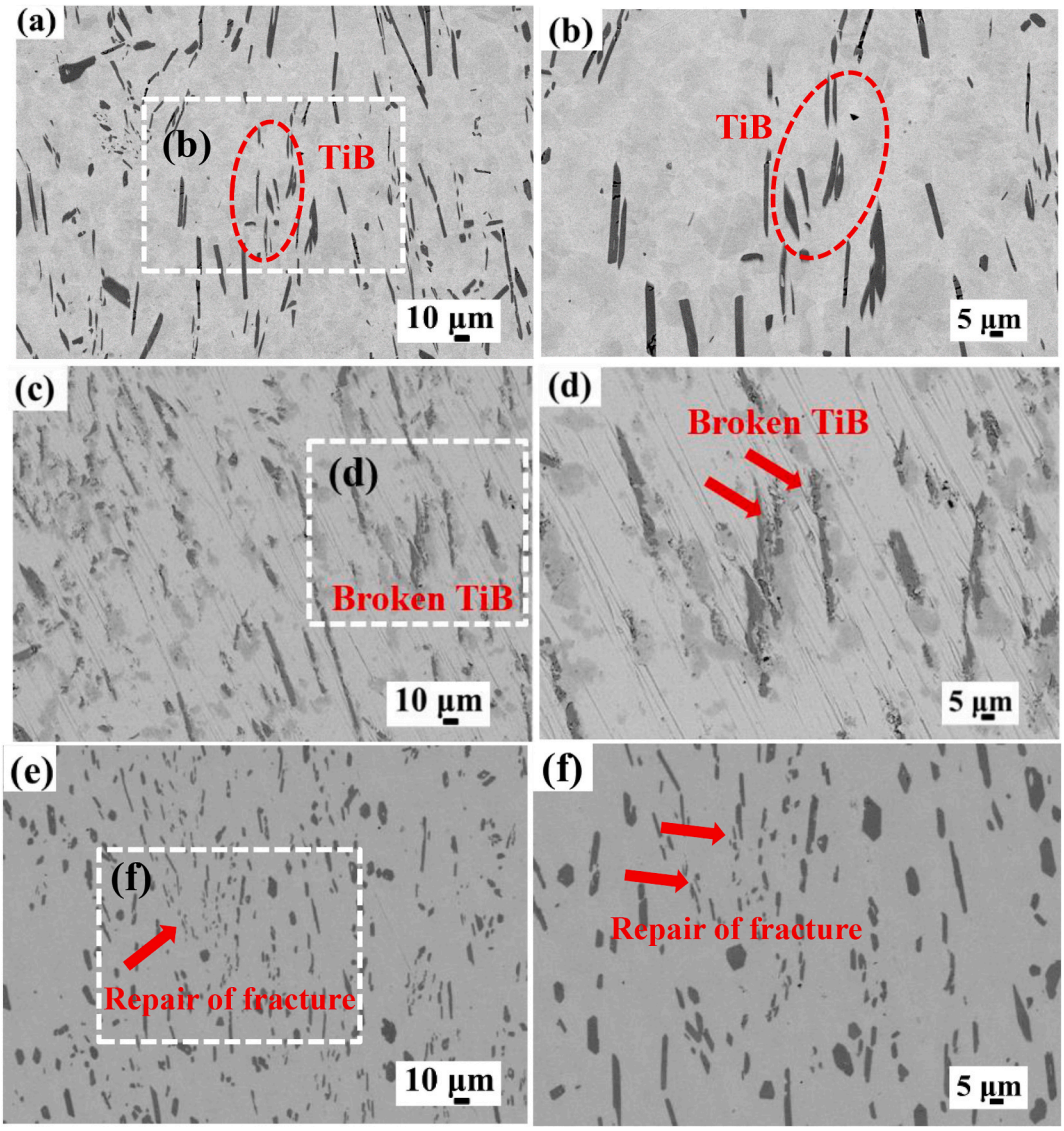

Fig. 2. Distribution of TiB on low-magnification SEM images for specimens: (a) No.1, (c) No.2, (e) No.3, and on high-magnification SEM images for specimens: (b) No.1, (d) No.2, (f) No.3.

emission rates of 0.15 and 0.23. The Hall current sensor externally connected to the electroshocking instrument is used for computer signal collection. The experimental instruments include an electroshocking instrument, the infrared thermal imager that monitors the temperature changes of the sample in real time, the Hall current sensor externally connected to the electroshocking instrument, and the computer connected to the Hall current sensor to collect current and pulse data.

2.2. Microstructure characterization

The specimens were cut by wire-electrode cutting after EST for microstructure characterization. The specimens were prepared by standard metallographic method, and the specimens were mounted and the surface were ground by sandpapers. Then the specimens were polished by a mixed solution containing OPS and H_2O_2 (V_{OPS}: $V_{H2O2} = 3:2$), in which the OPS solution was a SiO_2 suspension. The microstructure of TiB and α phase before and after EST were observed by SEM (Zeiss Ultra Plus, Germany) under a voltage of 10 kV, and the characterization area at middle position (M) is shown in Fig. 1(b). The specimens for TEM characterization were prepared using focused ion beam (FIB), and the current of FIB was set as 0.79 nA. The specimen contained both the matrix and TiB reinforcement, and the TEM observation area is shown in Fig. 1(b). The dislocations on phase boundaries and the element distribution were characterized and analyzed by Talos F200S TEM (FEI, USA). The TEM spot resolution was 0.25 nm, the resolution was 0.12 nm, the electron gun acceleration voltage was 200 kV, and the minimum spot size was 0.3 nm. Furthermore, the high-resolution atomic image characterization was performed on Titan Cubed Themis G2 300 (THERMO FISHER SCIENTIFIC). All experimental results were analyzed and discussed in detail. Meanwhile, the grain size, grain orientation and texture were characterized using the EBSD attachment on SEM (Zeiss Ultra Plus, Germany), and the characterization area was also the M area shown in Fig. 1(c). Before EBSD characterization, the specimens were polished via electrolytic polishing, and both the matrix and TiB reinforcement were characterized. In addition, the scanning area was 250 μm × 150 μm, and the step size of 0.5 μm was selected to detect the size variation of matrix and TiB before and after EST.

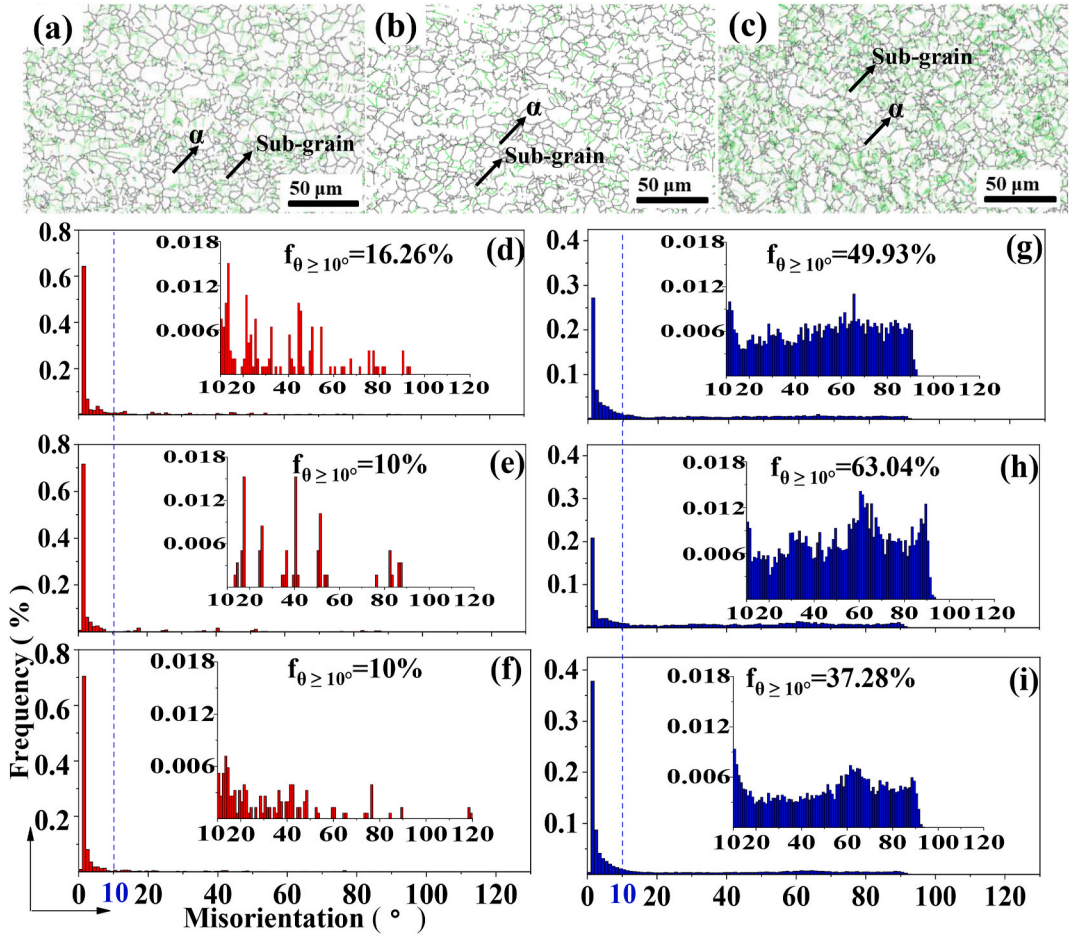

Fig. 3. (a), (b) and (c) grain boundary misorientation distributions of specimen No.1, No.2 and No.3 respectively; (d), (e), (f) statistics of TiB and (g), (h) and (i) statistics α grain boundary misorientation in specimen No.1, No.2 and No.3 respectively.

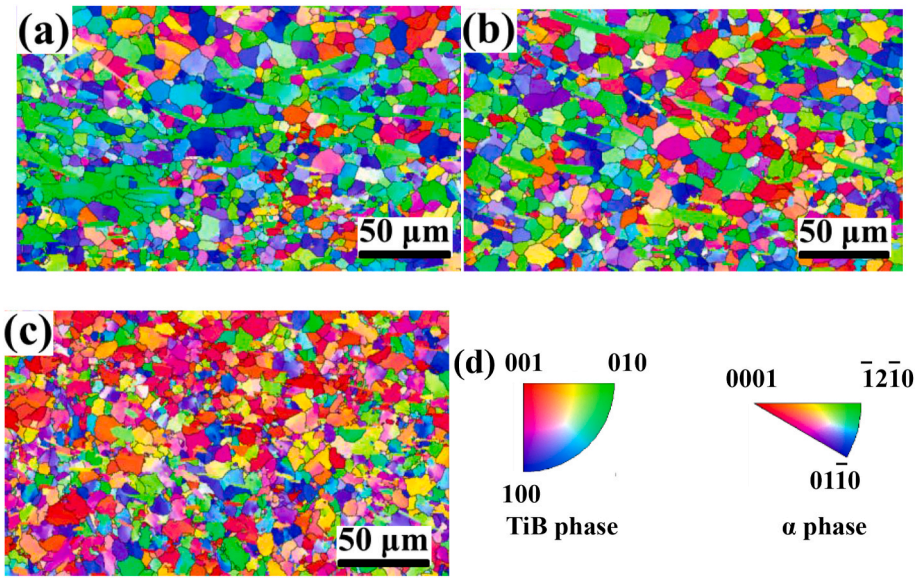

Fig. 4. (a)–(c) the grain orientation maps of specimen No.1, No.2 and No.3 respectively; (d) the standard orientation of α and TiB phases.

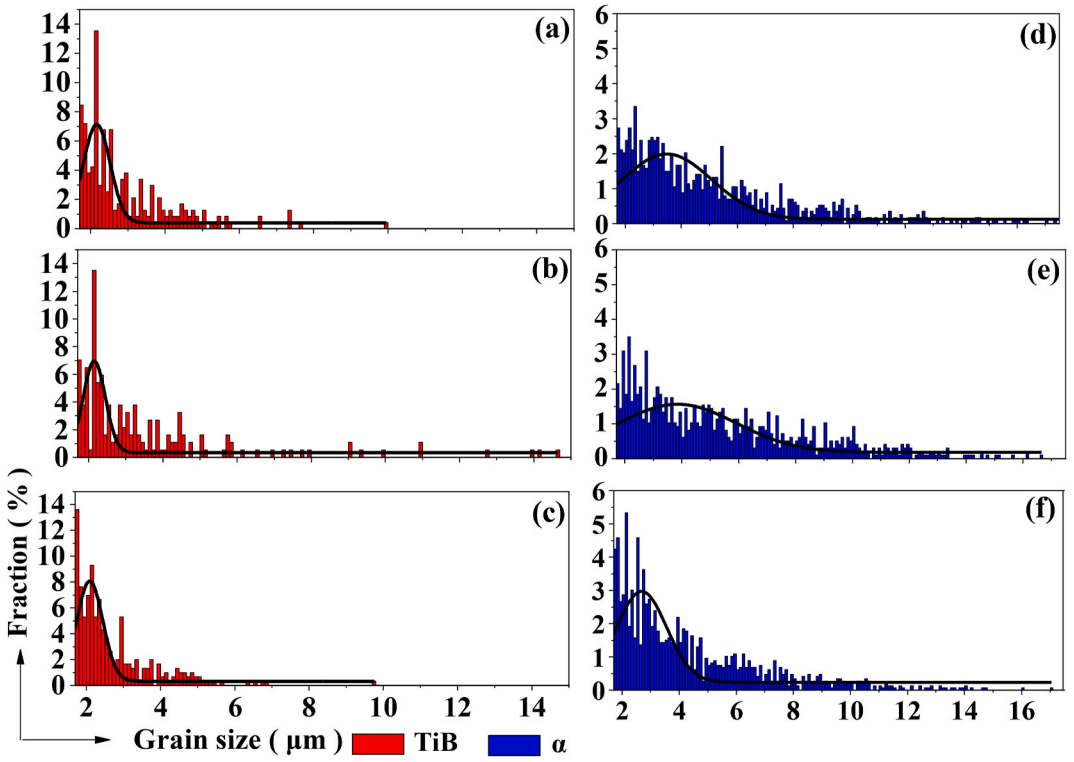

Fig. 5. (a), (b) and (c) show the equivalent diameter statistics of TiB in specimen No.1, No.2 and No.3 respectively; (d), (e) and (f) show the diameter statistics of α grains in specimen No.1, No.2 and No.3 respectively.

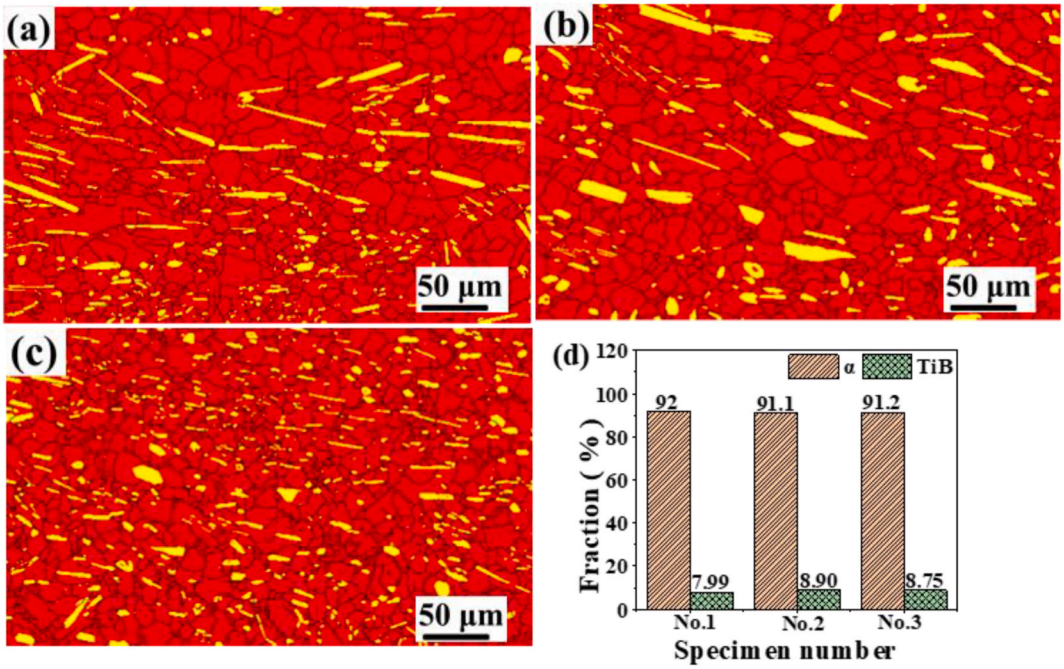

Fig. 6. (a), (b) and (c) show the phase distributions of specimen No.1, No.2 and No.3 respectively (the red areas represent α phase, and the yellow areas represent TiB phase); (d) the phase contents in specimens No.1, No.2 and No.3, respectively.

3. Results and discussion

3.1. Microstructure of specimens before and after EST

Fig. 2 shows the distribution of TiB before and after EST in M area, Fig. 2 (a), (c) and (e) are low-magnification SEM images, and (b), (d) and (f) are high-magnification SEM images. As seen from the distribution of TiB in No.1 (Fig. 2(a) and (b)), TiB is short-fiber-shaped along the axial direction and is unevenly distributed in the matrix. After EST in No.2 (in Fig. 2(c) and (d)), TiB is fractured and refined, and the distribution of TiB is relatively uniform. The interface cracks are introduced, resulting in formation of defects. This is due to the thermal and athermal effects of

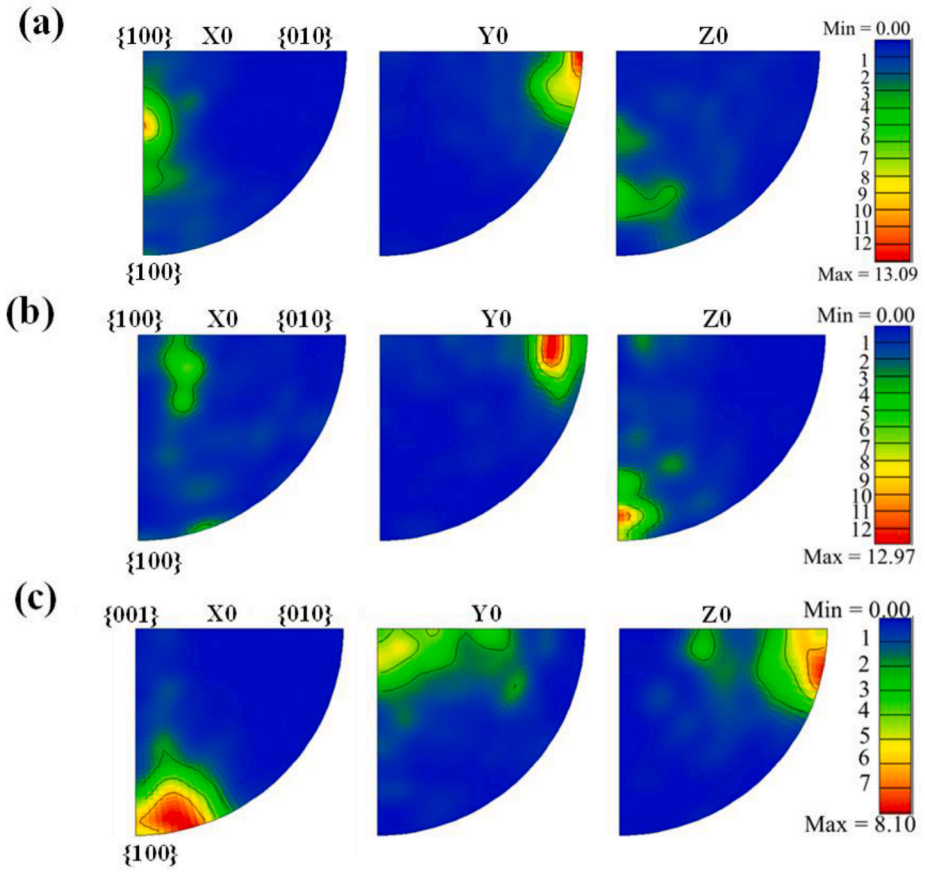

Fig. 7. Inverse pole figures (IPF) of TiB phase in specimen: (a) No.1, (b) No.2 and (c) No.3.

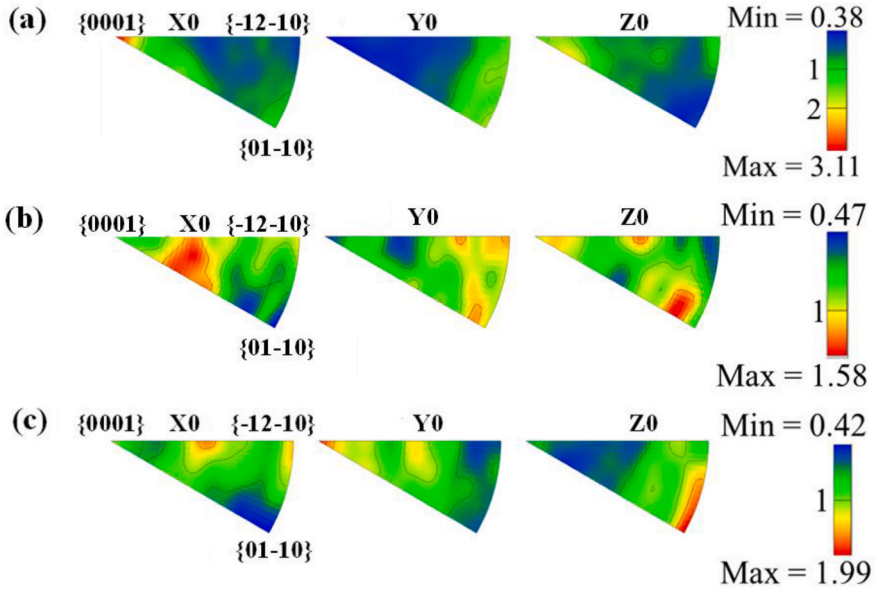

Fig. 8. Inverse pole figures (IPF) of α phase in specimen: (a) No.1, (b) No.2 and (c) No.3.

EST. In thermal effect, EST generated high energy pulse which caused the Joule thermal effect. In athermal effect, high energy pulse current caused the targeting effect and the selective effect. The energy is concentrated in TiB tip and TiB broken under the extrusion of matrix. In No.3, under the applying of EST plus external loading, the interface cracks are repaired under the effect of external loading. In TiB/Ti–2Al–6Sn, it mainly contains TiB and α phase, few β phase can be found [33]. After EST, the best refinement effect of TiB is shown in No. 3, which was under the simultaneous effect of EST and external loading (in Fig. 2(e) and (f)).

In order to investigate the influence mechanism of EST on the matrix and TiB, EBSD is utilized to analyze the grain boundary misorientation,

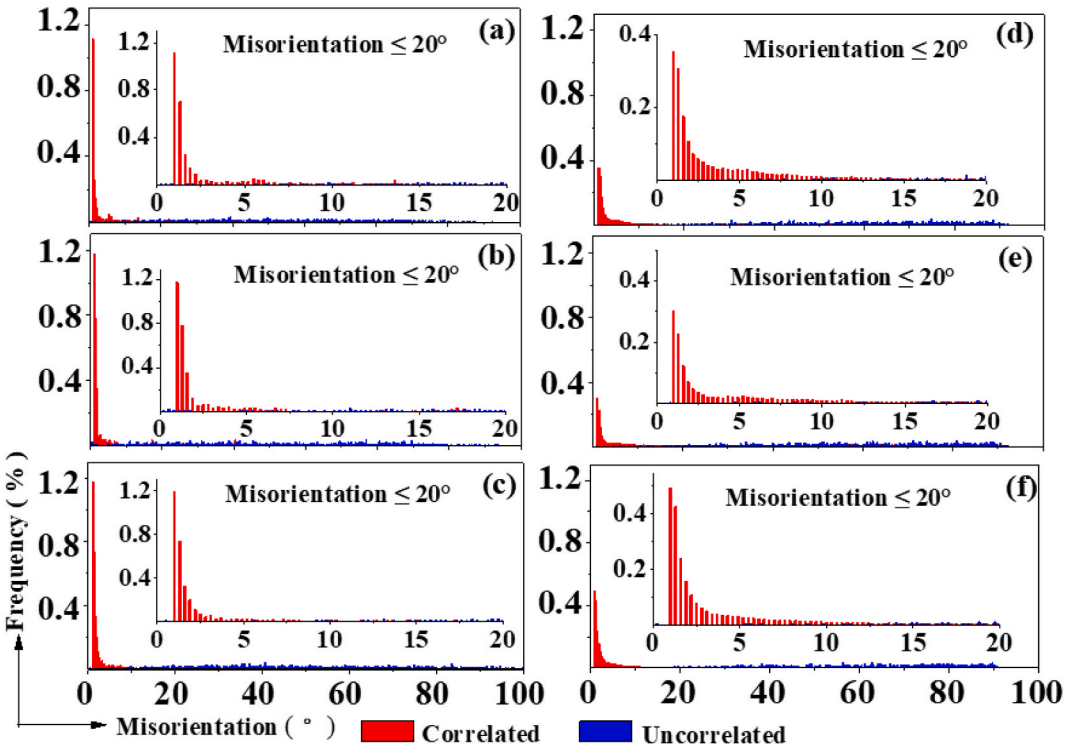

Fig. 9. (a)–(c) the statistics of TiB correlated and uncorrelated boundary orientation difference angles in specimen No.1, No.2 and No.3 respectively; (d)–(f) the statistics of α correlated and uncorrelated boundary misorientation angles in specimen No.1, No.2 and No.3 respectively.

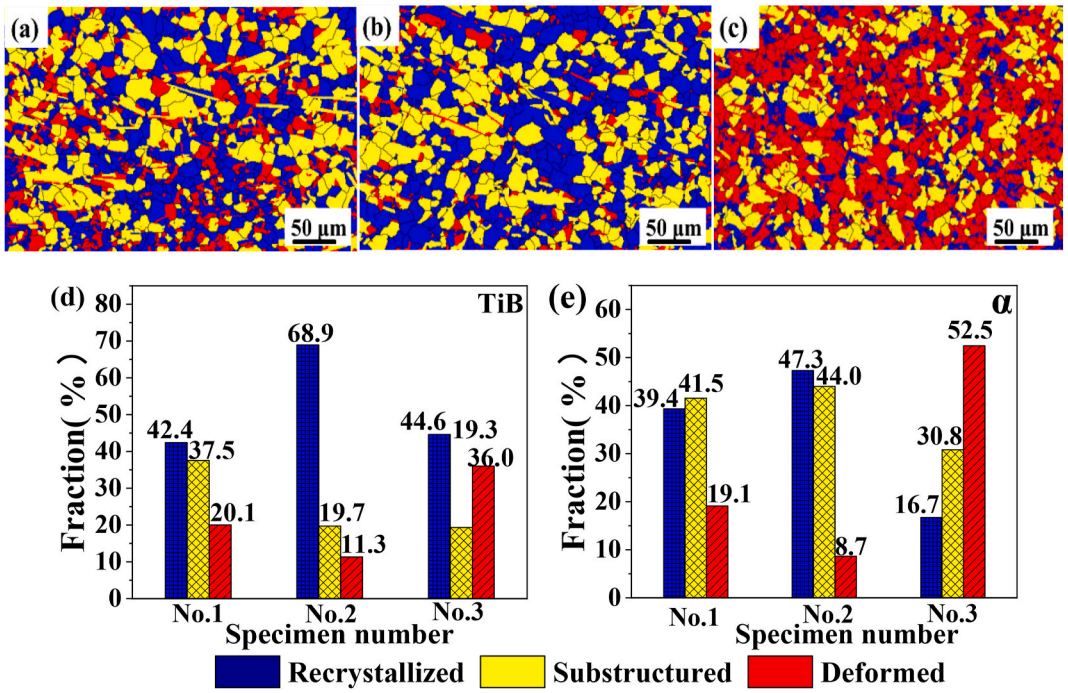

Fig. 10. (a)–(c) EBSD images of recrystallization, substructure and deformation phases of α and TiB in specimen No.1, No.2 and No.3 respectively; and the statistics of recrystallization, substructure and deformation phases of (d) TiB and (e) α phases in specimen No.1, No.2 ad No.3 respectively.

grain size, grain orientation and texture. The phase contents of specimens are also analyzed and discussion in the following sections.

3.2. Distribution of grain size and grain boundary misorientation

Fig. 3(a)–(c) show the distribution of grain boundary of specimens No.1, No.2 and No.3. It can be seen from Fig. 3(d)–(f) that the HAGBs percentages of TiB in No.2 (10 %) and No.3 (10 %) are reduced compared to No.1 (16.26 %). The LAGBs percentages of TiB in No.2 (90 %) and No.3 (90 %) are larger than that in No.1 (83.74 %). The LAGBs is composed of dislocations. The increase of LAGBs indicates that the dislocation density increases after EST [37]. This is mainly due to the

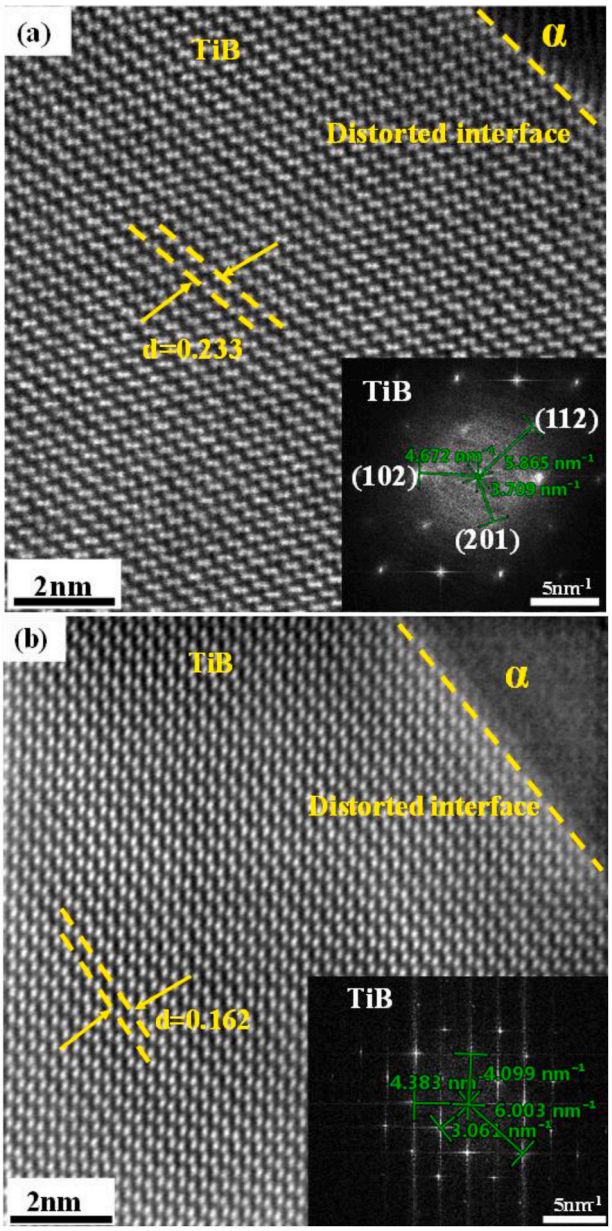

Fig. 11. Atomic images of TiB near the TiB/matrix interface and the corresponding selected area electron diffraction patterns of specimen: (a) No.1 and (b) No.3.

introduction of a large number of defects in TiB/matrix interface after EST [33]. In No. 2, interface cracks are introduced after EST. The effect of EST plus external loading in No. 3 can make crack repair without introducing new defects. So, the HAGBs of TiB in No. 3 do not change significantly.

Fig. 3(d)–(f) show the HAGBs ratio of α in No. 1 is 49.93 %, and that of No. 2 is increased to 63.04 %. This is mainly due to the growth of α under the Joule heating effect produced by EST [38]. The growth of α is dominated by the migration of grain boundaries, transforming from LAGBs to HAGBs [39]. Therefore, the ratio of α HAGBs increases. In No. 3, the proportion of α HAGBs is reduced to 37.28 %. This is because that the α recrystallizes when EST and external loading work together to produce a large number of sub-grains, which leads to an increase in LAGBs percentage and the smaller α size [40]. In addition, the dispersed TiB is conducive to the generation of sub-grain boundaries [41,42].

Fig. 4(a)–(c) show the orientation of grains in specimens No. 1, No. 2 and No. 3. The grain orientation map is mainly composed of TiB and α phase. Comparing Fig. 4(a) and (b), the orientation of TiB in No. 2 has changed after EST. Because TiB reinforcements are fractured after EST. Especially in No.3, the orientation of TiB is changed substantially while 0.3 MPa external loading is applied during EST, and the TiB particles are refined and their orientation becomes uniform, which are ascribed to the effects of EST and external loading. In addition, the α size becomes larger in No. 2, but it decreases significantly in No. 3 after applying external loading.

Fig. 5 shows the grain size distribution in the middle of three specimens. As seen from Fig. 5, the average size of TiB in No. 1 is 2.95 μm, and the average size of α is 2.42 μm. Compared with No.1, the average size of TiB in No.2 is reduced from 2.95 μm to 2.40 μm, which is ascribed to the refinement of TiB after EST. The average size of α grains increases from 2.42 to 3.24 μm, the potential reason is that the Joule heating effect introduced by EST promotes the growth of α grains [35,36,43]. In addition, compared with No.2, the average size of TiB in No.3 is increased, which may be influenced by some large and unrefined TiB. In No.3, the average size of α is reduced to 2.53 μm, which indicates that EST plus the external loading under 0.3 MPa can make α be refined. The thermal effect, athermal effect and external loading produced by EST refine the TiB particles. The decrease in α grain size is mainly due to the recrystallization of α under the extrusion of external loading during EST, which can produce a large number of sub-grains [40]. This is consistent with the results obtained in Fig. 4.

3.3. Phase content

The phase content of TiB and α phase can be obtained accurately according to EBSD results shown in Fig. 6. Fig. 6(a)–(c) shows the phase distribution of specimens No. 1, No. 2 and No. 3. The yellow area represents the TiB phase while the red area represents the α phase. The α phase is equiaxed. The phase content distributions of three specimens are shown in Fig. 6 (d). It can be observed from Fig. 6(a)–(c) that the TiB in No. 1 is short-fibrous and the size is larger and unevenly distributed. In No. 2, the TiB fractures and is refined, and the arrangement has been deflected. The large-size TiB has decreased after EST, which is consistent with the SEM results observed in Fig. 2(c)and (d). In No. 2, the α size becomes larger, which is consistent with the statistical results in Figs. 5 and 4. In No. 3, it apparent that the TiB is refined significantly and evenly distributed in the matrix, and the α grain size becomes smaller obviously, due to the combined effect of thermal stress and external loading generated during EST.

In Fig. 6(d), the phase content variation of TiB and α phase has been indicated. The content of α phase slightly decreases from 92 % (in No.1) to 91.1 % (in No.2) and 91.2 % (in No.3). By contrast, the TiB content increases slightly from 7.99 % (in No.1) to 8.90 % (in No.2) and 8.75 % (in No.3). Compared with No. 1, the contents of TiB phase and α phase in No. 2 and No. 3 show little variation. The above results verify that no new phase is formed after EST [36].

3.4. Texture analyses

Considering that the variation of grain size and grain orientation would influence the texture distribution, the inverse pole figures (IPF) of TiB and α phase are obtained via EBSD and shown in Fig. 7 and Fig. 8 to further analyze the texture variation. As seen from the IPF of TiB (Fig. 7 (a)), the maximum texture intensity of TiB in No. 1 is 13.09 and the intensity of {010} orientation is largest. Compared with No.1, the texture intensity of No.2 is reduced. As shown in Fig. 7 (b), the maximum texture intensity is 12.97, the intensity of {100} orientation becomes stronger, and the texture direction is parallel to the Z_0 direction. The possible reason for this is that TiB fractures and deflects after EST, the orientation of TiB is redistributed, and the fractured TiB no longer shows the same orientation as the original TiB [33,42]. Moreover, the decrease in texture intensity in No.2 verifies the refinement and redistribution of TiB after EST. No. 3 shows the smallest texture

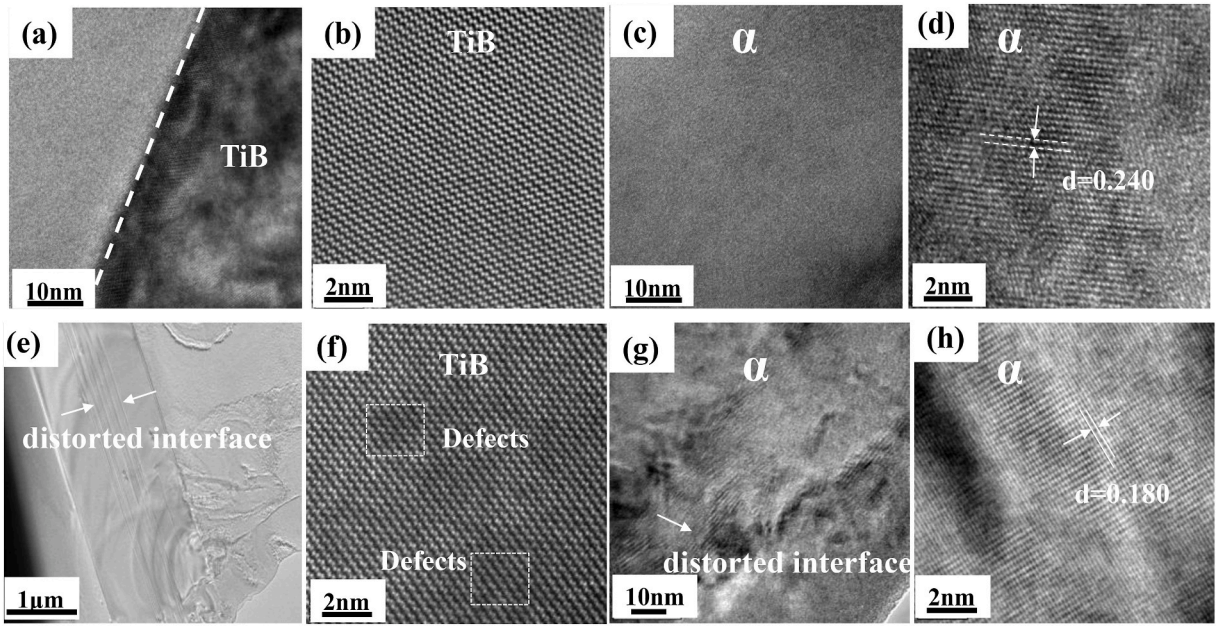

Fig. 12. (a)–(d) TEM images and corresponding HRTEM images of TiB and α interplanar spacing in No.1, (e)–(h) TEM images and corresponding HRTEM images of TiB and α interplanar spacing in No.3.

intensity after EST plus the external loading. As shown in Fig. 7 (c), the maximum texture intensity is 8.10, and both the intensities of {100} and {010} orientation become stronger, and the texture directions are parallel to the X_0 and Z_0 directions, respectively. Besides, the texture of {001} orientation parallel to the Y_0 direction also exists. Compared with No.2, the texture in No.3 emerges along three directions, and the intensity decreases significantly, which indicates the TiB in No.3 shows a better refinement and a more uniform distribution under EST plus external loading. These results are consistent with the microstructure variation shown in Fig. 2 and in our previous work [33].

Fig. 8 shows the texture distribution of α grains before and after EST. As shown in Fig. 8 (a), the maximum texture intensity of α in No.1 is 3.11 along the {0001} direction. Compared with No. 1, the texture intensity of No. 2 becomes lower. As shown in Fig. 8 (b), the maximum texture intensity is 1.58 and the intensity of {0001} texture becomes weaker, which is parallel to the X_0 direction. However, the texture intensity of {01–10} orientation becomes stronger, which is parallel to the Z_0 direction. The texture of α has changed from the original {0001} orientation to {01–10} orientation. The possible reason is ascribed to the growing α under EST, which is due to the thermal and athermal effects by EST [35,44,45]. Besides, compared with No. 2, the texture intensity of α phase in No. 3 increases slightly, from 1.58 to 1.99. The potential reason is that the α grains are deformed slightly under the external load of 0.3 MPa. In addition, the dispersed TiB is conducive to the generation of sub-grain boundaries, which can provide enough nucleation sites for α recrystallization [41,46]. The orientation between sub-grains may have a certain correlation [47]. Therefore, the α texture intensity of No. 3 increases, and the intensity of {01–10} orientation becomes weak, which is also related to the refinement and orientation variation of TiB.

Fig. 9(a)–(c) show the distribution of misorientation angles of correlated and uncorrelated boundaries of TiB in specimens No.1, No.2 and No.3. The distribution of misorientation angles of correlated and uncorrelated boundaries of α in No.1, No.2 and No.3 are shown in Fig. 9 (d)–(f). The red histograms indicate that the boundary misorientation angles are correlated, and the blue histograms indicate that the boundary misorientation angles are uncorrelated. All LAGBs show correlation, mainly because the LAGBs are distributed inside the grains belonging to the same parent phase. After EST with 0.06 s in No.2, the correlation and uncorrelation of the misorientation angles between TiB and α boundary do no show significant change (Fig. 9 (b) and (e)). The grain boundaries with correlation are mainly distributed in LAGBs, and there is no bias angle preference selection in HAGBs. The main reason is that TiB is refined, α is recrystallized, and the misorientation angles of grain boundaries from the same parent phase are correlated. After the coupled effect of EST and external loading, the correlation and uncorrelation of TiB boundary misorientation angles change not significantly (Fig. 9 (c)). The main reason is that the TiB originates from the same parent phase. The increase in the frequency of α boundary misorientation angle correlation is attributed to the combined action of EST and external loading (Fig. 9 (f)). As shown in Figs. 4 and 5, α is deformed, the size of α is significantly refined, and a large number of refined α subgrains come from the same parent phase, so the frequency of α boundary misorientation angle correlation increases.

Fig. 10(a)–(c) displays the recrystallization images of α and TiB phases in specimens No.1, No.2 and No.3. The blue area represents the recrystallization phase, the yellow area represents the substructure phase, and the red area represents the deformation phase. The statistics of recrystallization, substructure and deformation phases of TiB and α phase in these three specimens are shown in Fig. 10(d) and (e). Compared with No.1, the proportion of the recrystallized region of No.2 increases, and the area of the substructure region and the deformation region decreases, mainly due to the refinement of TiB, and the increase of α size. During recrystallization, the areas of substructure and deformed regions decrease, and the proportion of recrystallized regions increases. Compared with No.2, the recrystallization and substructure phase of No.3 are significantly reduced, and the deformation phase of α phase is significantly increased, the recrystallized and substructure phases are significantly reduced, while the grain refinement and the external loading lead to a significant increase in the deformation phase.

Fig. 11 shows the atomic images of TiB and TiB/matrix interface of specimens No. 1 and No. 3, and the corresponding selected area electron diffraction (SAED) patterns are shown. The interplanar spacing of TiB in No. 1 (before EST) and No. 3 (after EST plus external loading) is 0.233 nm (Fig. 11(a)) and 0.162 nm (Fig. 11(b)) respectively. It can be found that the interplanar spacing of TiB near the interface is changed after EST, which indicates that lattice distortion occurs after EST plus 0.3 MPa external loading.

Fig. 12 illustrates the TEM and HRTEM images of α and TiB phases in

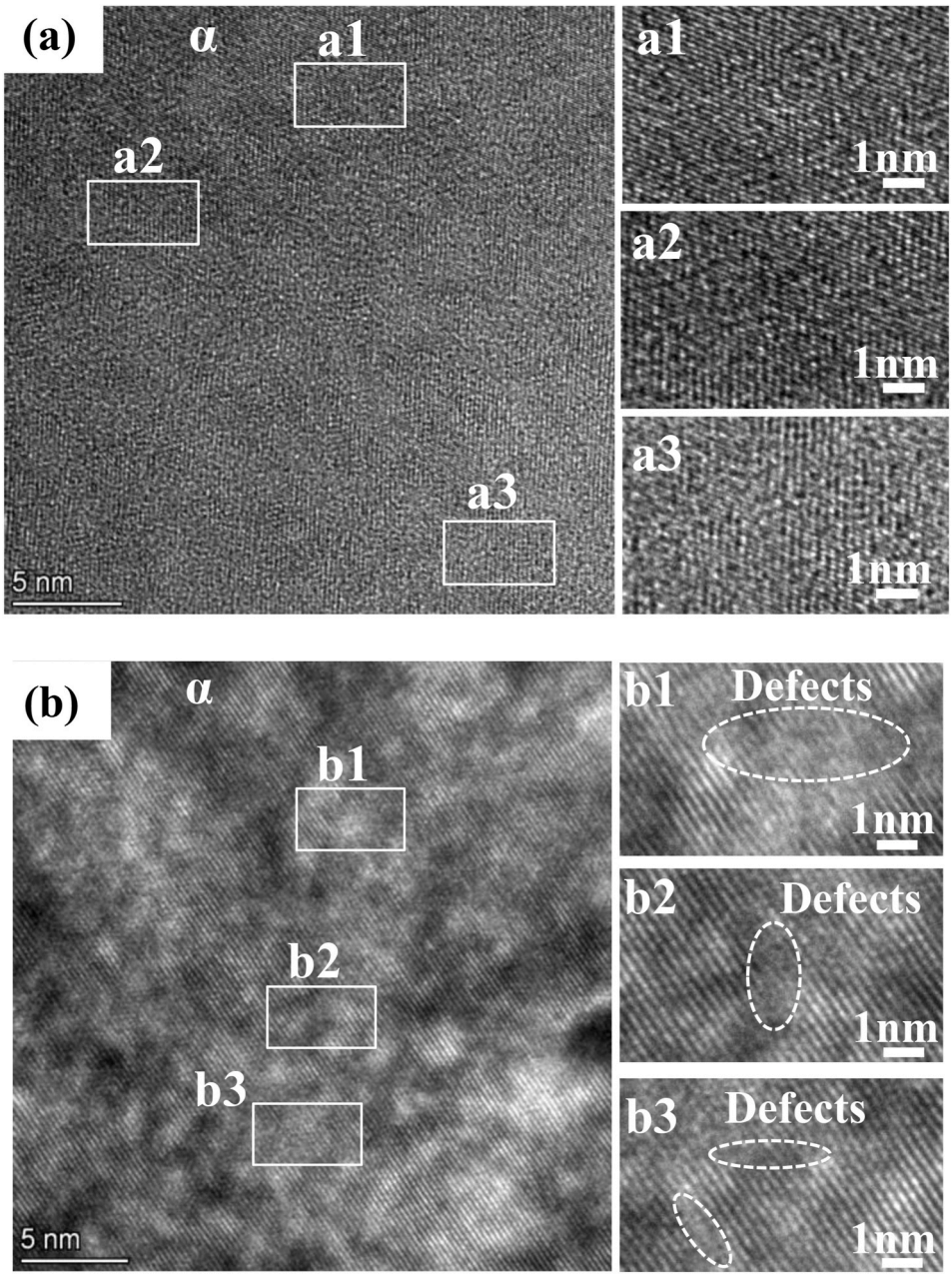

Fig. 13. (a) HRTEM images of α phase in No.1, (b) HRTEM images of α phase and defects in No.3.

No.1 and No.3. Fig. 12(a)–(d) shows the HRTEM images of TiB and α in No.1. In No.1, the TiB/matrix interface shows a good contact, as shown in Fig. 12(a), and there is no stacking fault in TiB, as shown in Fig. 12(b). There is no defects in the α interplanar spacing is 0.240 nm. Fig. 12(e) and(f) shows the HRTEM images of TiB and α in No.3. As observed in Fig. 12 (e), the stacking faults are formed in TiB in No. 3, and the lattice distortion are introduced in the α phase (Fig. 12 (f)), indicating that the combined effect of EST and external loading result in the formation of stacking faults in TiB and the lattice distortion in α phase [48]. As seen from the HRTEM images of α in No.3 (Fig. 12(g) and(h)), the width of α interplanar spacing decreases from 0.240 nm to 0.180 nm after EST, and TiB produces defects, which is due to the combined effect of EST and external loading.

Fig. 13(a) and(b) shows the HRTEM images of α phase in No.1 and No.3. It can be observed that there is few defects in No.1 before EST (Fig. 13 (a)). However, there are a large number of defects in No.3 after EST plus external loading (Fig. 13 (b)). The variation of interplanar spacing and the induce of defects after EST plus external loading are ascribed to the deformation of α phase and TiB. After mere EST, TiB is refined and deflected under the extrusion of the α matrix. The α locally grows and deforms under the thermal and athermal effects of EST, resulting in the variation of orientation and texture strength. While after EST plus the external loading, the refinement and deformation of TiB and α become more evident, which influences the recrystallization, substructure and deformation phases of TiB and α. Due to more apparent refinement and deformation of TiB and α, the lattice distortion and the variation of interplanar spacing are induced. These effects can be attributed to the thermal and athermal effects of EST, and the deformation effect of external loading.

4. Conclusions

In this work, the texture evolution of TiB/Ti–2Al–6Sn TMC after EST plus external loading were studied, and the mechanism of TiB/

Ti–2Al–6Sn after EST plus external loading is revealed. The TMC after EST plus external loading can modify the texture intensity, indicating that the advantages of EST plus external loading can be applied to change the microstructure of TMCs, which aims to provide new ideas and methods for the processing of TMCs. And some important results are summarized as follows:

(1) After EST plus external loading, TiB refinement was more uniform, and a large number of sub-grains were induced, which refined the α grains. The variation in HAGBs proportion related to the change of the size of TiB and α.
(2) After single EST, the HAGBs proportion of α increased from 49.9 % to 63.0 % due to the growth of α under the thermal effect of EST. But, after EST plus external loading, the proportion of α HAGBs was decreased to 37.28 %. This reduction was attributed to the substantial formation of sub-grains resulting from α phase recrystallization, which increased the proportion of LAGBs.
(3) After single EST, TiB orientation was redistributed, leading to the decrease in texture strength. After EST plus external loading, the texture strength decreased significantly, indicating that TiB exhibited better refinement and more uniform distribution under the combined action of EST and external loading.
(4) After single EST, the orientation of α phase show significant variation, and the texture intensity decreased. This can be attributed to the local growth and deformation of the α phase under EST. After EST plus external loading, the texture intensity of α phase not change significantly compared with the specimen after a single EST, because the external loading was only 0.3 MPa.
(5) The variation in interplanar spacing and the induce of defects observed after EST plus external loading can be ascribed to the deformation of α phase and TiB. The more significant refinement and deformation of TiB and α result in lattice distortion and changes in interplanar spacing. These effects can be attributed to both the thermal and athermal effects of EST, and the deformation effect of external loading.

All results show that EST plus the external loading can modify the texture of TMCs. EST provides a simple and efficient method for manipulating the microstructure of TMCs. It is supposed to improve the mechanical properties of TMCs.

Contribution of each author

Yaya Wu: Investigation, Data curation, Writing - original draft.
Yan Wen: Investigation, Data curation, Writing - original draft.
Anan Guo: Investigation, Writing - review & editing.
Jian Zhou: Investigation, Writing - review & editing.
Fei Yin: Investigation, Writing - review & editing.
Lechun Xie: Methodology, Writing - original draft, Writing - review & editing.
Liqiang Wang: Methodology, Writing - original draft, Writing - review & editing.
Lin Hua: Supervision; Writing - review & editing.
Weijie Lu: Writing - review & editing.
Lai-Chang Zhang: Writing - review & editing.

Data availability

The raw/processed data required to reproduce these findings cannot be shared at this time as the data also forms part of an ongoing study.

Declaration of competing interest

The authors declare that they have no known competing financial interests or personal relationships that could have appeared to influence the work reported in this paper.

Acknowledgements

This work was financially supported by Major Research Plan of the National Natural Science Foundation of China (Grant No. 92266102), National Natural Science Foundation of China (Grant No. 52271135), Natural Science Foundation of Hubei Province (Grant No. 2022CFB492), Knowledge Innovation Program of Wuhan -Basic Research (No.2022010801010174), "Chu Tian Scholar" project of Hubei Province (CTXZ2017-05), Overseas Expertise Introduction Project for Discipline Innovation, China (B17034) and Innovative Research Team Development Program of Ministry of Education of China (IRT_17R83).

References

[1] Tjong SC, Mai Y-W. Processing-structure-property aspects of particulate-and whisker-reinforced titanium matrix composites. Compos Sci Technol 2008;68(3–4):583–601.
[2] Morsi K, Patel V. Processing and properties of titanium–titanium boride (TiBw) matrix composites—a review. J Mater Sci 2007;42(6):2037–47.
[3] Ozerov M, Stepanov N, Kolesnikov A, Sokolovsky V, Zherebtsov S. Brittle-to-ductile transition in a Ti–TiB metal-matrix composite. Mater Lett 2017;187:28–31.
[4] Tjong S, Ma Z. Microstructural and mechanical characteristics of in situ metal matrix composites. Mater Sci Eng R Rep 2000;29(3–4):49–113.
[5] Zhang L-C, Xu J, Eckert J. Thermal stability and crystallization kinetics of mechanically alloyed Ti C/ Ti-based metallic glass matrix composite. J Appl Phys 2006;100(3):033514.
[6] Xie L, Wang L, Wang K, Yin G, Fu Y, Zhang D, et al. TEM characterization on microstructure of Ti–6Al–4V/Ag nanocomposite formed by friction stir processing. Materialia 2018;3:139–44.
[7] Wang L, Xie L, Shen P, Fan Q, Wang W, Wang K, et al. Surface microstructure and mechanical properties of Ti-6Al-4V/Ag nanocomposite prepared by FSP. Mater Char 2019;153:175–83.
[8] Huang L, Geng L, Peng H. Microstructurally inhomogeneous composites: is a homogeneous reinforcement distribution optimal? Prog Mater Sci 2015;71:93–168.
[9] Huang L, Geng L. Discontinuously reinforced titanium matrix composites[M]. City: Springer; 2017.
[10] Hill D, Banerjee R, Huber D, Tiley J, Fraser HL. Formation of equiaxed alpha in TiB reinforced Ti alloy composites. Scripta Mater 2005;52(5):387–92.
[11] Sun X, Han Y, Cao S, Qiu P, Lu W. Rapid in-situ reaction synthesis of novel TiC and carbon nanotubes reinforced titanium matrix composites. J Mater Sci Technol 2017;33(10):1165–71.
[12] Nandwana P, Hwang JY, Koo MY, Tiley J, Hong SH, Banerjee R. Formation of equiaxed alpha and titanium nitride precipitates in spark plasma sintered TiB/Ti–6Al–4V composites. Mater Lett 2012;83:202–5.
[13] Sasaki TT, Fu B, Torres K, Thompson GB, Srinivasan R, Cherukuri B, et al. Nucleation and growth of α-Ti on TiB precipitates in Ti–15Mo–2.6Nb–3Al–0.2Si–0.12B. Phil Mag 2011;91(6):850–64.
[14] Roy S, Suwas S, Tamirisakandala S, Srinivasan R, Miracle DB. Microstructure and texture evolution during β extrusion of boron modified Ti–6Al–4V alloy. Mater Sci Eng, A 2012;540:152–63.
[15] Wen Y, Wu Y, Hua L, Xie L, Wang L, Zhang L-C, et al. Effects of shot peening on microstructure evolution and mechanical properties of surface nanocrystal layer on titanium matrix composite. Mater Des 2021;206:109760.
[16] Sen I, Gopinath K, Datta R, Ramamurty U. Fatigue in Ti–6Al–4V–B alloys. Acta Mater 2010;58(20):6799–809.
[17] Zhang W-J, Song X-Y, Hui S-X, Ye W-J, Wang W-Q. Phase precipitation behavior and tensile property of a Ti–Al–Sn–Zr–Mo–Nb–W–Si titanium alloy. Rare Met 2018;37(12):1064–9.
[18] Yu Y, Zhang W, Dong W, Han X, Pei C, Jiao X, et al. Research on heat treatment of TiBw/Ti6Al4V composites tubes. Mater Des 2015;73:1–9.
[19] Huang L, Xu H, Wang B, Zhang Y, Geng L. Effects of heat treatment parameters on the microstructure and mechanical properties of in situ TiBw/Ti6Al4V composite with a network architecture. Mater Des 2012;36:694–8.
[20] Huang L, An Q, Geng L, Wang S, Jiang S, Cui X, et al. Multiscale architecture and superior high-temperature performance of discontinuously reinforced titanium matrix composites. Adv Mater 2021;33(6):2000688.
[21] Wang B, Huang LJ, Hu HT, Liu BX, Geng L. Superior tensile strength and microstructure evolution of TiB whisker reinforced Ti60 composites with network architecture after β extrusion. Mater Char 2015;103:140–9.
[22] Ni DR, Geng L, Zhang J, Zheng ZZ. TEM characterization of symbiosis structure of in situ TiC and TiB prepared by reactive processing of Ti–B4C. Mater Lett 2008;62(4):686–8.
[23] Roy S, Suwas S. Microstructure and texture evolution during sub-transus thermomechanical processing of Ti-6Al-4V-0.1 B alloy: Part I. Hot rolling in (α+ β) phase field. Metall Mater Trans 2013;44(7):3303–21.
[24] Huang LJ, Geng L, Li AB, Yang FY, Peng HX. In situ TiBw/Ti–6Al–4V composites with novel reinforcement architecture fabricated by reaction hot pressing. Scripta Mater 2009;60(11):996–9.
[25] Lu W, Zhang D, Zhang X, Wu R, Sakata T, Mori H. HREM study of TiB/Ti interfaces in a TiB-TiC in situ composite. Scripta Mater 2001;44(7):1069–75.
[26] Saito T. The automotive application of discontinuously reinforced TiB-Ti composites. JOM 2004;56(5):33–6.

[27] Li H, Jia D, Yang Z, Liao X, Jin H, Cai D, et al. Effect of heat treatment on microstructure evolution and mechanical properties of selective laser melted Ti–6Al–4V and TiB/Ti–6Al–4V composite: a comparative study. Mater Sci Eng, A 2021;801:140415.
[28] Wu Y, Zhou X, Wang X, Lu Y, Peng M, Duan Y. Microstructure and some properties of powder-pack borided Ti–5Mo–5V–8Cr–3Al alloy with special attention to the microstructure at the interface TiB/substrate. Ceram Int 2022;48(17):24346–54.
[29] Yang A, Wu Y, Duan Y, Peng M, Zheng S, Li M, et al. The effect of alloying elements in Ti-5Mo-5V-8Cr-3Al alloy on growth kinetics of TiB whiskers in boride layer. Mater Des 2023;225:111478.
[30] Song X, Wang F, Qian D, Hua L. Tailoring the residual stress and mechanical properties by electroshocking treatment in cold rolled M50 steel. Mater Sci Eng, A 2020;780:139171.
[31] Wu W, Song Y, Wang Z, Ning S, Hua L. Solid phase transformation of Ti–6.6Al–3.4Mo alloy induced by electroshocking treatment. J Mater Sci 2020;55 (5):2245–55.
[32] Liu C, Xie L, Qian D, Hua L, Wang L, Zhang L-C. Microstructure evolution and mechanical property response of TC11 titanium alloy under electroshock treatment. Mater Des 2021;198:109322.
[33] Xie L, Wu Y, Yao Y, Hua L, Wang L, Zhang L-C, et al. Refinement of TiB reinforcements in TiB/Ti-2Al-6Sn titanium matrix composite via electroshock treatment. Mater Char 2021;180:111395.
[34] Xie L, Guo H, Song Y, Hua L, Wang L, Zhang L-C. Novel approach of electroshock treatment for defect repair in near-β titanium alloy manufactured via directed energy deposition. Metall Mater Trans 2021;52(2):457–61.
[35] Xie L, Guo H, Song Y, Liu C, Wang Z, Hua L, et al. Effects of electroshock treatment on microstructure evolution and texture distribution of near-β titanium alloy manufactured by directed energy deposition. Mater Char 2020;161:110137.
[36] Xie L, Liu C, Song Y, Guo H, Wang Z, Hua L, et al. Evaluation of microstructure variation of TC11 alloy after electroshocking treatment. J Mater Res Technol 2020; 9(2):2455–66.
[37] Zaefferer S, Kuo JC, Zhao Z, Winning M, Raabe D. On the influence of the grain boundary misorientation on the plastic deformation of aluminum bicrystals. Acta Mater 2003;51(16):4719–35.
[38] Lu Z, Guo C, Li P, Wang Z, Chang Y, Tang G, et al. Effect of electropulsing treatment on microstructure and mechanical properties of intermetallic Al3Ti alloy. J Alloys Compd 2017;708:834–43.
[39] Huang S, Ma Y, Zhang S, Youssef SS, Qiu J, Wang H, et al. Nonuniform recrystallization and growth behavior of β grains dominated by grain misorientation and interfacial energy in metastable β titanium alloy. Metall Mater Trans 2018;49(12):6390–400.
[40] Doherty RD, Hughes DA, Humphreys FJ, Jonas JJ, Jensen DJ, Kassner ME, et al. Current issues in recrystallization: a review. Mater Sci Eng, A 1997;238(2):219–74.
[41] Qiu P, Han Y, Le J, Huang G, Lei L, Xiao L, et al. Particulate induced dynamic globularization/recrystallization and unique superplasticity in TiB/near-α Ti matrix composites. Mater Char 2020;167:110458.
[42] Roy S, Suwas S, Tamirisakandala S, Miracle DB, Srinivasan R. Development of solidification microstructure in boron-modified alloy Ti–6Al–4V–0.1B. Acta Mater 2011;59(14):5494–510.
[43] Gil FJ, Planell JA. Behaviour of normal grain growth kinetics in single phase titanium and titanium alloys. Mater Sci Eng, A 2000;283(1):17–24.
[44] Zeng L, Bieler TR. Effects of working, heat treatment, and aging on microstructural evolution and crystallographic texture of α, α′, α″ and β phases in Ti–6Al–4V wire. Mater Sci Eng, A 2005;392(1):403–14.
[45] Xu J, Zeng W, Zhang X, Zhou D. Analysis of globularization modeling and mechanisms of alpha/beta titanium alloy. J Alloys Compd 2019;788:110–7.
[46] Chen R, Tan C, Yu X, Hui S, Ye W, Lee Y. Effect of TiB particles on the beta recrystallization behavior of the Ti-2Al-9.2Mo-2Fe-0.1B metastable beta titanium alloy. Mater Char 2019;153:24–33.
[47] Gao X, Zeng W, Wang Y, Long Y, Zhang S, Wang Q. Evolution of equiaxed alpha phase during heat treatment in a near alpha titanium alloy. J Alloys Compd 2017; 725:536–43.
[48] Wen Y, Wu Y, Liu P, Xie L, Lu W. Residual stress distribution and microstructure characterization of particle reinforced titanium matrix composite after shot peening treatment: a review. Curr Nanosci 2021;17(2):194–222.